Isotopically resolved intermediate-mass fragment and light charged particle production from the reactions ^{40}Ar and ^{40}Ca with ^{58}Fe and ^{58}Ni at $E_{beam}=33$ and 45 MeV/nucleon

H. Johnston, T. White, B. A. Li, E. Ramakrishnan, J. Winger, D. J. Rowland, B. Hurst, F. Gimeno-Nogues, D. O'Kelly, Y.-W. Lui, and S. J. Yennello

Cyclotron Institute, Texas A&M University, College Station, Texas 77843-3366

(Received 9 April 1997)

Isotopically resolved intermediate-mass fragments and light charged particles have been detected from the reactions ^{40}Ar and ^{40}Ca with ^{58}Fe and ^{58}Ni at $E_{beam}=33$ and 45 MeV/nucleon. There is an angular dependence to the isotopic ratios. A moving source analysis shows that fragments emitted at $\Theta_{lab}=40°$ can be attributed primarily to a composite source while the fragments emitted at backward angles are primarily from a targetlike source. The results are compared to predictions of QMD, BUU, and GEMINI. QMD generally reproduces the charge distribution and energy spectra and has partial success with the isobaric ratios when the system is chemically equilibrated. All of the models have difficulty reproducing the isotopic ratios when the system is not chemically equilibrated. [S0556-2813(97)05710-5]

PACS number(s): 25.70.Mn, 24.10.Nz, 24.10.Pa, 25.70.Pq

INTRODUCTION

Recently much attention has been focused on understanding the degree of thermal [1–5], chemical [6–8], and shape [10,11] equilibration achieved in intermediate-energy heavy-ion collisions. In many treatments of intermediate energy heavy-ion collisions equilibrium has been assumed. The assumption of equilibrium is a cornerstone of hybrid model calculations [12,13] where dynamics have been taken into account in a collision phase, but an equilibrated residue is assumed in the second stage of statistical fragmentation. The recent excitement about a ''caloric curve'' is based upon a formalism that assumes chemical and thermal equilibrium [14]. It is important to define the boundaries over which these assumptions are valid. Studies of the equilibration of the isospin degree of freedom can help define one segment of the boundary conditions.

The isobaric ratios of intermediate-mass fragments (IMF's) measured at 40° from central collisions of ^{40}Ar, ^{40}Ca with ^{58}Fe, ^{58}Ni show a characteristic change from being dependent only on the composite projectile+target system at $E_{beam}=33$ MeV/nucleon to also having a dependency on the entrance channel at 45 MeV/nucleon thus signaling the onset of the nonequilibration of the isospin degree of freedom [7]. This paper will present a more detailed study of the reactions that straddle that transition. The angular dependence of the isotopic ratios, a moving source analysis of the data, and comparison to the results predicted by QMD [15], BUU [16], and GEMINI [17] will be presented.

EXPERIMENTAL DETAILS

All data were acquired at the Texas A&M University Cyclotron Institute. Beams of ^{40}Ar and ^{40}Ca were extracted from the K500 cyclotron. These beams were first passed through a thin aluminum foil resulting in charge distributions that were strongly peaked at fully stripped. The fully stripped beams were then transported to the target at the center of the neutron ball [18]. Targets were 2 mg/cm^2 ^{58}Fe and ^{58}Ni. Six gas ionization-Si-Si-CsI detectors [19] were placed inside the scattering chamber of the neutron ball at laboratory angles of 11°, 44°, 72°, 100°, 128°, 148° as shown in Fig. 1. These telescopes provided detection of charged particles with charge resolution for $Z=1$ to 16 and A resolution up to $Z=9$. The neutron ball detected the coincident neutrons with 82% efficiency as measured with a ^{252}Cf source. Further experimental details can be found elsewhere [7].

Characteristic energy spectra were observed for the IMF's; the cross section decreases approximately exponentially with the energy of the fragment. The exponential slope becomes less steep for higher Z fragments. Further discussion of these spectra can be found later in this paper; for now we will integrate these spectra to extract fragment yields. The mass resolution for IMF's arises from the excellent energy resolution of the silicon detectors, and thus is present for fragments that punch through the first silicon and stop in the second silicon. For fragments that punch through the second silicon there is mass resolution up through He. Therefore the range of energies over which we are able to measure the isotopic resolution is determined by the stopping power of the silicon detectors. The extracted ratios are integrated from the energy where the particle with the higher linear energy transfer LET punches into the second silicon to the energy where the particle with the lower LET punches through the second silicon detector. This is determined for each isotopic and isobaric pair presented. The error bars are purely statistical and do not include any systematic errors that may be present. We have investigated the effects of the limits of integration and the results for the ^{10}Be/^{10}B ratios at $\Theta_{lab}=40°$ are shown in Table I. The extracted ratios are not significantly affected by changing either the lower limit or the upper limit of integration. This indicates that at 40° we are not sensitive to a preequilibrium component, which has been shown [20] to be reflected in the isotopic ratio as a function of the energy of the fragment observed.

ANGULAR DISTRIBUTIONS OF ISOTOPIC RATIOS

The previously published data [7] concentrated on central collisions at $\Theta_{lab}=40°$, where the concentration at that laboratory angle was chosen to emphasize the most central collisions. In Fig. 2 the ratio of each carbon isotope relative to

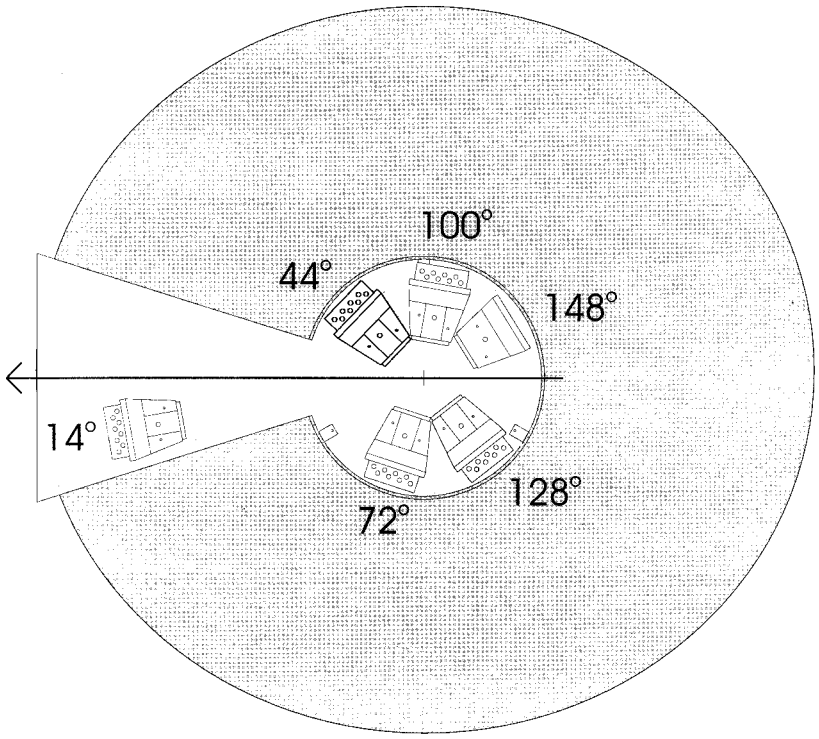

FIG. 1. Experimental setup showing placement of six gas-ionization chamber telescopes within the scattering chamber of the neutron ball.

the total carbon detected for each of the reacting systems measured at a particular lab angle is plotted versus the isotope number. Within each isotope grouping the compound systems are ordered from the system with the most number of neutrons to the least number of neutrons. The reaction of Ar+Fe is the left-hand bar with the highest total number of neutrons and produces the lowest fraction of $^{11}C/^{tot}C$ at all angles. The Ca+Ni system with the lowest number of neutrons produces the largest fraction of $^{11}C/^{tot}C$ at all angles. The middle two bars represent the mixed systems of Ar+Ni and Ca+Fe having the same total number of protons and neutrons that are divided differently between the projectile and target. For these two compound systems the $^{11}C/^{tot}C$ ratios lie between the extreme systems. The behavior of $^{14}C/^{tot}C$ mirrors that of $^{11}C/^{tot}C$ with the Ar+Fe system producing the largest fraction of $^{14}C/^{tot}C$ and the Ca+Ni system producing the smallest. This results in a global behavior in which the fraction of isotopes with fewer numbers of neutrons relative to the total has an increasing slope as a function of the charge to mass ratio of the combined system while the isotopes with larger numbers of neutrons have a decreasing slope.

Another interesting feature of this plot is that the fractions of $^{11}C/^{tot}C$ and $^{14}C/^{tot}C$ are roughly equal for the forward angles while the $^{11}C/^{tot}C$ is more dominant than the $^{14}C/^{tot}C$ at the central angles. The $^{11}C/^{14}C$ averaged over all systems is 0.81 for the forward angles while it increases to 2.2 for the more central angles. So the fragments detected at forward angles have more neutrons, regardless of the entrance channel relative to those detected from more central collisions. This is consistent with a scenario where the fragments at central angles are associated with more violent collisions that give off more neutrons and thus have fewer neutrons available in the residue for fragmentation products.

While it would be extremely informative to look at the angular distribution of these heavy fragments at more backward angles there are not significant numbers of carbon fragments beyond the 48° telescope for all systems. So in order to address how yield ratios change over a broader range of angles we must turn to helium fragments. Since lighter fragments, especially ^{4}He, are susceptible to feeding from the deexcitation of primordial prefragments we may expect that any signatures of the initial dynamics would be damped due to this secondary decay. However, a change in isotope ratios as a function of angle has been seen previously for helium fragments [8]. The isotopic ratio of ^{4}He/^{3}He was plotted with respect to the N/Z of the compound system in Fig. 3 where $(N/Z)_{cs}$ is

TABLE I. The $^{10}Be/^{10}B$ ratio measured at $\Theta_{lab}=40°$ as extracted from the data for different limits of integration.

	$^{10}Be/^{10}B$		
	65:150	65:130	80:150
	33 MeV		
Ca+Ni	0.39±0.01	0.40±0.01	0.36±0.02
Ca+Fe	0.67±0.02	0.69±0.02	0.63±0.02
Ar+Ni	0.64±0.02	0.65±0.03	0.59±0.03
Ar+Fe	1.04±0.03	1.06±0.03	0.93±0.04
	45 MeV		
Ca+Ni	0.48±0.02	0.48±0.02	0.43±0.02
Ca+Fe	0.72±0.02	0.73±0.02	0.65±0.02
Ar+Ni	0.55±0.02	0.56±0.02	0.50±0.03
Ar+Fe	0.89±0.04	0.89±0.04	0.80±0.04

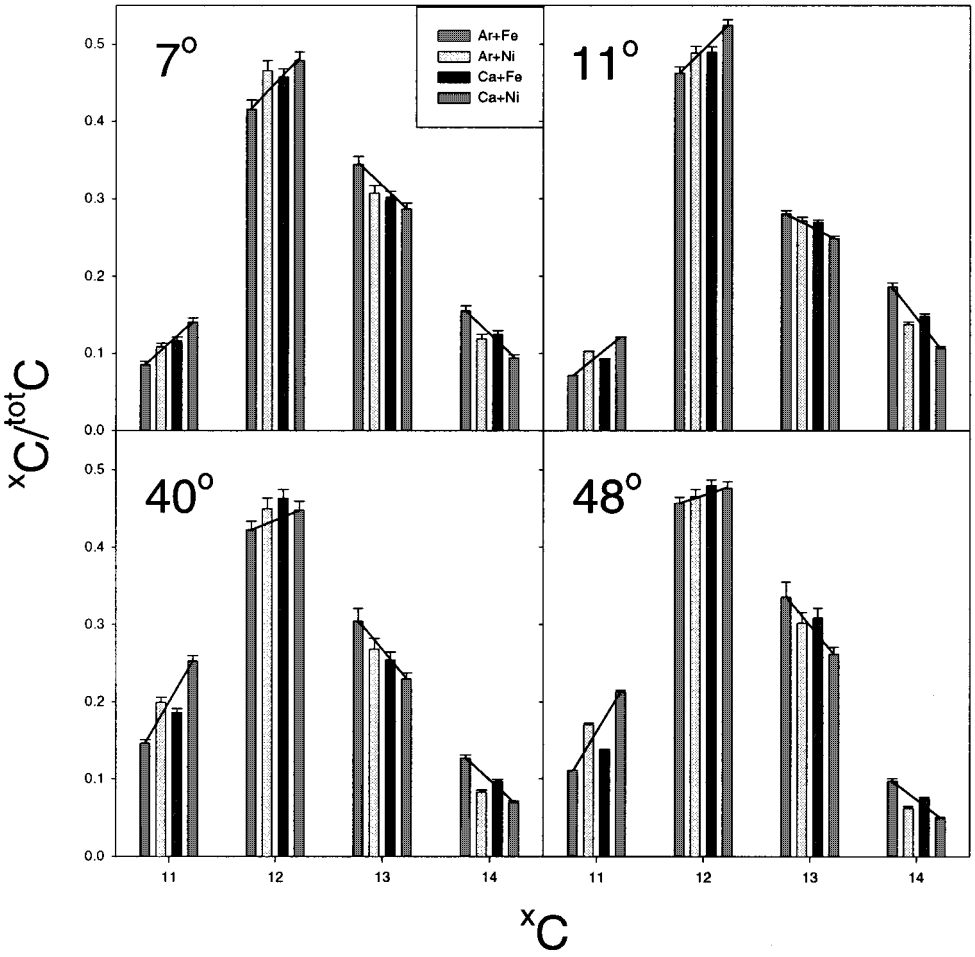

FIG. 2. Ratio of carbon isotopes to total carbon detected at each of four laboratory angles: 7°, 11°, 40°, and 48°.

$$\left(\frac{N}{Z}\right)_{\rm cs}=\frac{(N_{\rm projectile}+N_{\rm target})}{(Z_{\rm projectile}+Z_{\rm target})}. \tag{1}$$

$N_{\rm projectile(target)}$ and $Z_{\rm projectile(target)}$ are the number of neutrons and protons in the projectile(target). At 40° a single line cannot fit all the data points at $E_{\rm beam}=33$ and 45 MeV/nucleon. This trend is maintained in all but the $E_{\rm beam}=33$ MeV/nucleon ratios at 104°. This behavior suggests that there might be contributions from collisions at noncentral impact parameters at these angles. In fact the ratio at 152° can largely be attributed to a source whose composition is largely controlled by the composition of the target, rather than a composite projectile+target system.

MOVING SOURCE ANALYSIS

Fitting energy spectra with a moving source formalism has been used to determine the relative contribution from various sources at different angles [21–23]. Following this approach, a moving source analysis was performed on the measured cross sections. Since the forward-moving projectile remnant has essentially no contribution to the spectra measured at angles as backward as $\Theta_{\rm lab}=40$; the spectra were fitted with the sum of two Maxwellian functions representing a targetlike and a central source. This is consistent with the data of Wile *et al.* [22] that showed a significant contribution from the projectile like source at forward angles but essentially no contribution backward of 30° in the lab for the asymmetric $N+$Ag system at comparable energies.

The midrapidity source was assumed to be the residue formed in a central collision that then emits fragments with a Maxwellian energy distribution

$$P(E)=N(E-B_c)\exp\frac{-(E-B_c)}{T_c}, \tag{2}$$

where N is the normalization, B_c is the Coulomb barrier, T_c is the temperature, and E is energy. The source moved in the beam direction and emitted isotropically in its rest frame.

The targetlike source is based upon the idea that IMF's emitted at backward angles are from a system in which the interaction time was greater than one nuclear rotation period. The origin of the targetlike source,

$$P(E)=N_t(2E-p)e^{-(E/T_t)}\,\mathrm{erf}\left[\frac{(p-2E)}{2\sqrt{pT_t}}+2\left(\frac{pT_t}{\pi}\right)^{1/2}e^{[(p^2+4E^2)/4pT_t]}\right], \tag{3}$$

was based upon the scission point model of Nix [24] which was modified by Moretto [25]. It was characterized by a mean velocity, a Coulomb barrier B_t, and a temperature T_t. An additional parameter, p, permitted the evolution of spectral shapes with fragment charge.

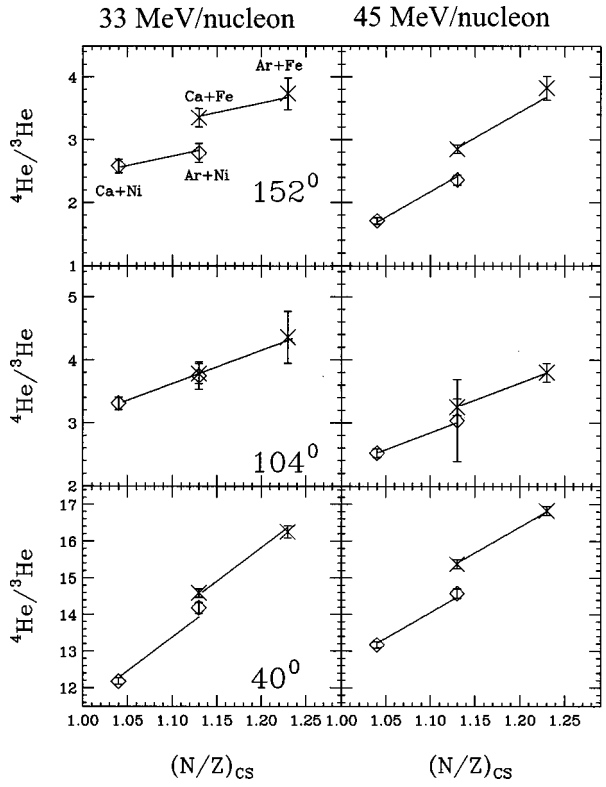

FIG. 3. Isotopic ratios plots for ^{4}He/^{3}He as a function of the N/Z of the compound system at $E_{\text{beam}}=33$, 45 MeV/nucleon, at $\Theta_{\text{lab}}=40°$, 104°, and 152°.

For the reaction ^{40}Ar+^{58}Ni at $E_{\text{beam}}=33$ and 45 MeV/nucleon, the fit parameters were determined by first fitting the inclusive He spectra detected at backward angles with the target source, Eq. (3). The parameters $T_t=6.3$ MeV (8 MeV) and $\nu_t=0.01c$ ($0.024c$) were fixed for $E_{\text{beam}}=33$ (45) MeV/nucleon; then He spectra detected at intermediate angles (40°, 48°, 68°, 76°) were fit with the sum of the two sources. In order to approximate the best values of the parameters for the central source, the velocity and temperature of the central source were frozen and the remaining IMF's were fit. This procedure was repeated iteratively until all of the IMF's were fit with $\nu_c=0.046c$ ($0.085c$) and $T_c=19$ MeV (23.5 MeV) for the 33 (45) MeV/nucleon data. This description fits the data quite well.

The left side of Fig. 4 shows the fitted kinetic energy spectra for He at $E_{\text{beam}}=33$ MeV/nucleon. The solid line is the sum of the contributions from the central and targetlike sources. The dotted line is the contribution from the targetlike source while the dashed line is the contribution from the central source. At backward angles (152°), the energy spectra are fit exclusively with the target source. Except at very low energies, the He spectra are fit almost exclusively with a single source at intermediate angles. Figure 5 is the fitted kinetic energy spectra for IMF's $Z=2-6$ at 40° and 76° at $E_{\text{beam}}=33$ MeV/nucleon. For $Z>3$ the target source did not contribute to the energy spectra. This indicates that at 40°, the IMF's are emitted from a single central source.

The right side of Fig. 4 shows the fitted kinetic energy spectra for He at $E_{\text{beam}}=45$ MeV/nucleon. Like the reaction at 33 MeV/nucleon, at backward angles the He spectra are fit.

The right side of Fig. 4 shows the fitted kinetic energy spectra for He at $E_{\text{beam}}=45$ MeV/nucleon. Like the reaction at 33 MeV/nucleon, at backward angles the He spectra are fit exclusively with the targetlike source. However, at forward angles, the targetlike source makes a small contribution to the energy spectra. While at 33 MeV/nucleon the targetlike source did not contribute to the IMF's energy spectra for $Z>3$, at 45 MeV/nucleon this is no longer the case, as displayed in the rightmost panels of Fig. 5. For Z's as great as 6 the targetlike source influenced the energy spectra at low energies. IMF's at 40° at 45 MeV/nucleon are emitted from both the targetlike source and the central source. However, the IMF's from the targetlike source are all low energy fragments. These low energy fragments from the targetlike source are stopped in the first silicon and do not overcome the energy threshold required to be included in the measured isotopic ratios.

NEUTRON MULTIPLICITIES

Neutrons detected with the neutron ball were used to differentiate between central and peripheral collisions. In many experiments the multiplicity of neutrons detected have been used as a measure of the centrality of a collision [26,27,9,10]. In a recent experiment of $E_{\text{beam}}=35$ MeV/nucleon ^{63}Cu with ^{197}Au it was shown the TAMU neutron ball has a much higher efficiency for neutrons from a compound nucleuslike source relative to projectilelike or preequilibrium sources. The multiplicity of neutrons was correlated with the excitation energy of the system [28]. However, it was recently shown for heavy symmetric reactions at a similar energy that while the number of neutrons detected could discriminate between central and peripheral collisions, it was less sensitive than the number of detected charged particles [29]. This was attributed to very peripheral binary collisions creating a ''background noise'' for the neutron multiplicity trigger. It seems the effectiveness of neutron multiplicity as a centrality trigger may be dependent on the asymmetry of the reaction. In order to estimate the effectiveness of this centrality trigger for our current data simulations (described in detail later in this paper) were run for ^{40}Ca+^{58}Fe at $E_{\text{beam}}=33$ MeV/nucleon. The calculated neutron multiplicity spectra are compared with the experimental measured spectrum in Fig. 6. The multiplicity of neutrons is much higher for the $b=0$ collision than the $b=5$ collision. By gating on the 10% of events with the highest neutron multiplicity we are clearly discriminating against peripheral events.

To determine the contributions to the fragment spectra from collisions at noncentral impact parameters the neutrons emitted in coincidence with fragments at 40° and 152° from a hybrid calculation of BUU/GEMINI, at $b=0$ fm and $b=5$ fm were recorded. The number of events was adjusted for geometrical cross sectional differences. A ratio was made between the number of events with a neutron multiplicity of at least 6, calculated at $b=0$ fm and the number of events with the same neutron multiplicity at $b=5$ fm. The ratios were determined to be 19.0 and 11.1 at 40° and 1.3 and 2.2 at 152° for $E_{\text{beam}}=33$ and 45 MeV/nucleon respectively. At intermediate angles, high neutron multiplicities are clearly outside the region in which $b=5$ fm contributes signifi-

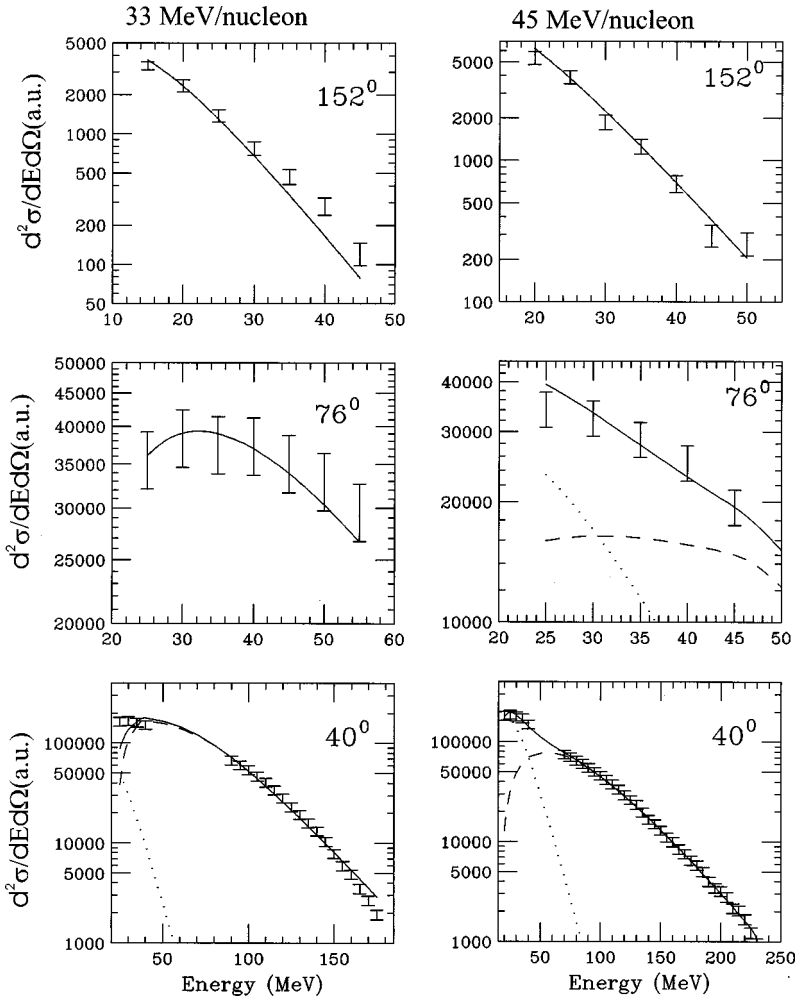

FIG. 4. Fitted He energy spectra at $E_{beam}=33$ MeV/nucleon (left) and 45 MeV/nucleon (right) for different angles. The dotted line is the contribution from the target source. The dashed line is the central source contribution and the solid line is the sum of the two sources.

cantly, but at backward angles the collisions at $b=5$ fm make a larger contribution to the neutron multiplicity. In addition to the neutron multiplicity comparisons the fragments were filtered for detector acceptance to investigate the contributions to the charge distribution from central versus midimpact parameter collisions. The $b=5$ collisions produced essentially no fragments with a charge greater than three in our 40° telescope.

To eliminate any contamination from the target source in the 40° yields, a coincident neutron multiplicity cut was made for the 10% highest neutron multiplicity events. Except at 40° for 33 MeV/nucleon the overall behavior of the helium ratios remain unchanged. Now at 40° the 33 MeV/nucleon ratios, can be fit with a single line as the Ca+Fe and the Ar+Ni are no longer statistically different. At 152° the isotopic ratios are still fit with two lines. The source fits showed that at 152° the energy spectra could be explained entirely by emission from a targetlike source. In addition, at backward angles, $b=5$ fm collisions make a greater contribution to the neutron multiplicity. While at intermediate angles the neutron multiplicity cut gates upon central collisions, at backward angles this same cut is actually not as discriminating toward this class of events. Therefore, the angle of the detector will affect what sources are contributing to the observed fragments. At intermediate angles the fragments appear to be originating from a composite source while at backward angles a targetlike source is the main contributor.

COMPARISON WITH MODEL PREDICTIONS

Using the statistical model GEMINI and the dynamical models of BUU and QMD theoretical calculations have been compared to the experimental results. While none of these models have yet evolved to the point that they properly account for all aspects of isospin dependence it is illustrative to compare their predictions with our data to determine how important these missing elements are. GEMINI was developed to treat the decay of a hot system and as such does not take into account the dynamical evolution of the system. The necessary inputs to GEMINI are the excitation energy, charge and mass number of the residue, which can be extracted from a BUU calculation. This method using a hybrid model to account for the dynamics, while still looking at the larger clusters in the data has been successful in reproducing some aspects of the data from the reaction of ^{139}La+^{27}Al at 45 MeV/nucleon [13]. Even so, this method fails to account for preequilibrium emission of complex fragments and its ability to reproduce the isospin of the emitted fragments has never been tested.

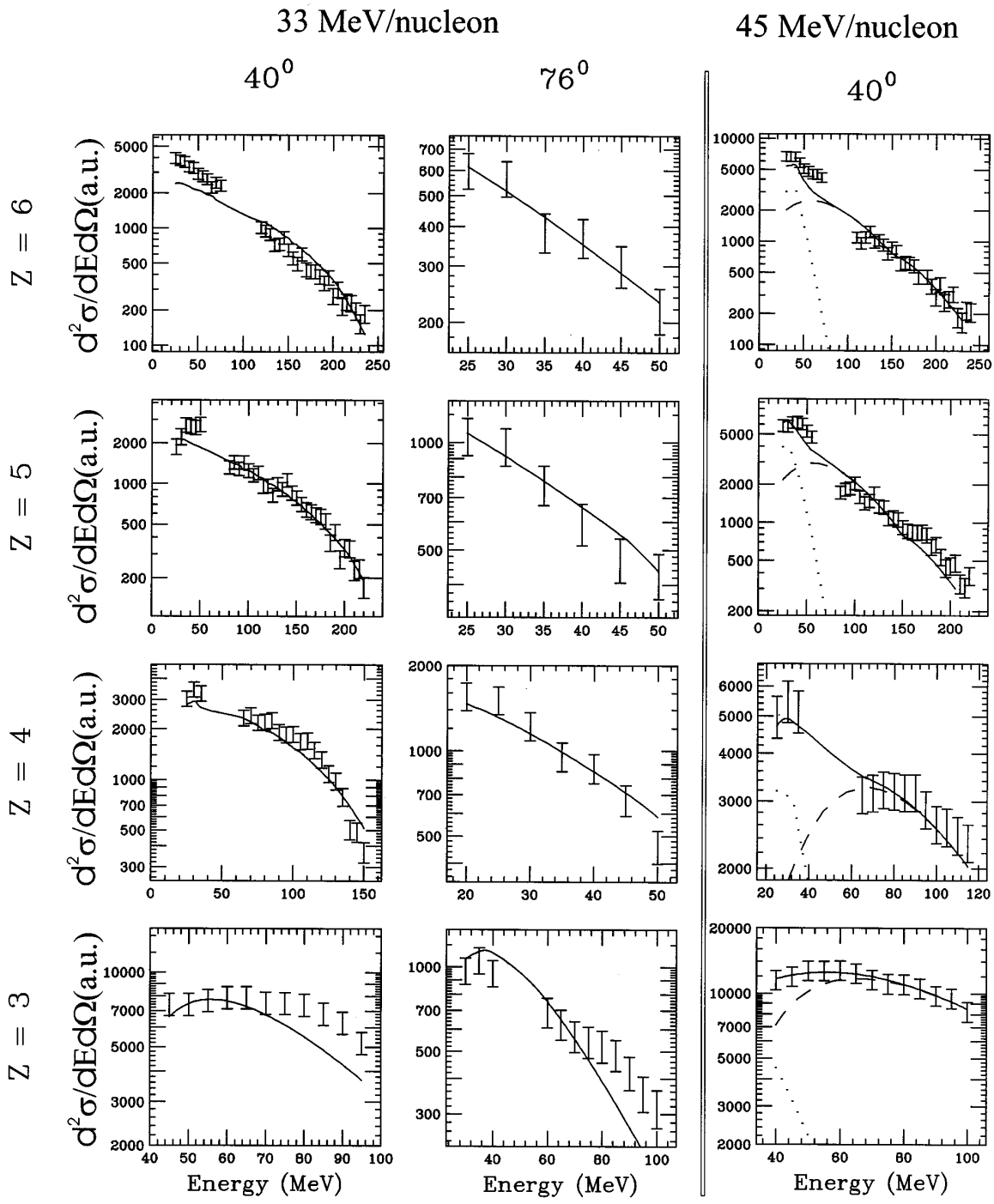

FIG. 5. Fitted energy spectra for Z's between 3–6 generated from the reaction ^{40}Ar+^{58}Ni at E_{beam}=33 MeV/nucleon at Θ_{lab}=40° and 76° and at E_{beam}=45 MeV/nucleon at Θ_{lab}=40°.

It has been shown that for the reaction ^{40}Ca+^{58}Fe at $E_{\text{beam}}=33$, 45 MeV/nucleon BUU predicts, at $b=0$, a single residue at 33 MeV/nucleon and a large residue with a small forward projectilelike residue at 45 MeV/nucleon [30]. Since experimentally there is a distribution of impact parameters, the residues from $b=0-3$ fm were calculated. The A, Z and excitation energy of the hot residue was computed at 140 fm/c with the constraint $\rho=\rho_0/8$. These residues were input to the code GEMINI and allowed to decay statistically. These results were filtered for the energy threshold and geometric acceptance of the detector.

Since there is some latitude in the calculation of E^* from BUU the results from the BUU/GEMINI coupling were also compared to the complete fusion limit with just GEMINI. The input parameters for using just GEMINI were derived from the system that arises from both complete fusion and complete momentum transfer of the target and projectile, as displayed in Table II. The residues were given an angular momentum of $\ell=0$. Like the BUU/GEMINI calculations, the results were filtered for the detector acceptance.

In addition to GEMINI and BUU coupled with GEMINI, results were also calculated using QMD. QMD simulates both evolution and fragmentation of a reacting system. However, QMD does not explicitly treat the isospin in either the

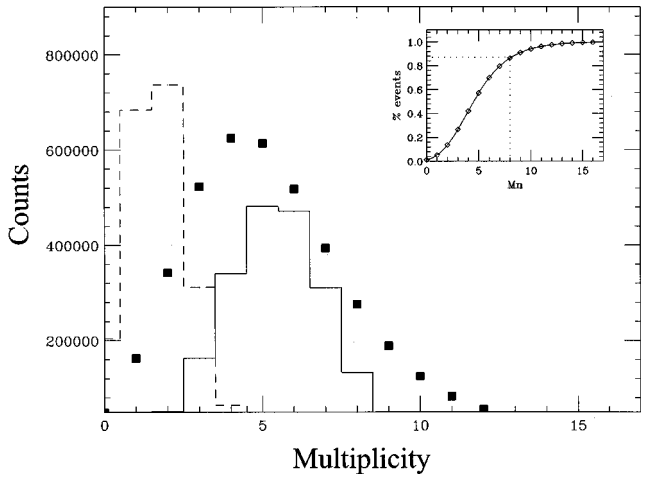

FIG. 6. The experimental neutron multiplicity in coincidence with a valid event (solid squares) in comparison to the distributions predicted by BUU/GEMINI at $b=0$ (solid histogram) and $b=5$ (dashed histogram) for $^{40}Ar+^{58}Ni$ at 33 MeV/nucleon. The inset shows the percent of events with a given multiplicity.

potential or the cross section, but it will conserve numbers of nucleons. In this way entrance channel effects that are due to nonequilibration of the entrance channel can possibly be observed. The statistical multifragmentation code (SMM) that is the afterburner for QMD has had some success in predicting the relative isotope detected from the collision of $p+Kr$ [31]. The projectile and target were allowed to collide with an impact parameter between $b=0-3$ fm. The results were filtered for the detector's acceptance and its angle.

Table II compares the residues determined by complete fusion with the residues predicted by BUU at $b=3$ fm and QMD at the end of the first stage for $b=0-3$ fm, for $E_{\text{beam}}=33$ and 45 MeV/nucleon. With complete fusion, the excitation energy and A of the residue do not change with the reacting system. Any differences in systems are due to the differing number of neutrons and protons in the residues. With the increased number of neutrons in the $^{40}Ar+^{58}Fe$ system, GEMINI should predict neutron-rich fragments relative to the fragments predicted for $^{40}Ca+^{58}Ni$. At $E_{\text{beam}}=33$ MeV/nucleon, the spread in N/Z for the BUU residues' is less than the spread of N/Z of the complete fusion system. Therefore GEMINI's fragment distribution, using the BUU residues, should not change as much from system to system.

QMD predicts a single residue with, on average, 11.2 light fragments, $\langle A\rangle=1.3$ and $\langle Z\rangle=0.65$ at $E_{\text{beam}}=33$ MeV/nucleon. At $E_{\text{beam}}=45$ MeV/nucleon, multiplicity of preequilibrium fragments increases to 14.4 with a similar average size and charge. The composition of the preequilibrium fragments changes a great deal across the systems at both $E_{\text{beam}}=33$ MeV/nucleon and $E_{\text{beam}}=45$ MeV/nucleon. While the N/Z of the prefragments increases with the N/Z of the reacting system, the composition of these fragments fails to contribute to the IMF fragment yields. Only 0.4% of events produced a prefragment with $Z>2$ at 40°. The N/Z of the residue changes significantly less than the N/Z of the complete fusion residues.

Figure 7 shows the experimental Z distributions in comparison to the distributions predicted by BUU coupled with GEMINI, GEMINI alone, and QMD for the reaction of $^{40}Ca+^{58}Fe$ at $E_{\text{beam}}=33$ and 45 MeV/nucleon for central collisions. The experimental Z distribution of fragments was determined by gating upon the events where the neutron multiplicity was in the 90th percentile and the fragment had enough energy to enter the first silicon detector but not enough energy to punch thru the CsI(Tl). The diamonds in Fig. 7 are the experimental data, the solid histogram is the BUU/GEMINI prediction and the dotted histogram is the QMD prediction. BUU/GEMINI's and QMD's Z distributions were normalized to the experimental data for $Z=5$ at 40°.

Overall, BUU/GEMINI closely approximates the experimental Z distribution at $E_{\text{beam}}=33$ MeV/nucleon (left side of the figure). At 6° (bottom left panel) BUU/GEMINI follows the experimental Z distribution closely. At larger angles BUU/GEMINI fails to reproduce the higher Z's At 40°, BUU/GEMINI fails for $Z>10$ and for 76° and 152° fails for $Z>3$. At $E_{\text{beam}}=45$ MeV/nucleon BUU/GEMINI agrees with the experimental results for $Z<10$ at 6° and 40° but at higher angles and higher Z's. BUU/GEMINI underpredicts the experimental values. At forward angles at both energies, QMD closely agrees with the experimental results but at angles greater than 76° QMD fails to produce any fragments. GEMINI calculates a distribution very similar to QMD's at forward angles, but at backward angles GEMINI's distribution is similar to BUU/GEMINI's.

The inclusive ^{7}Li energy spectrum (diamonds) is shown in Fig. 8. This spectrum was compared to the energy spectra calculated by QMD (dotted), BUU coupled to GEMINI (solid), and GEMINI alone (dashed). GEMINI predicts a Maxwellian distribution that peaks at about 40 MeV/nucleon and tails off rapidly whether its input is from complete fusion or BUU. For energies between 40 and 80 MeV/nucleon, QMD's prediction for the ^{7}Li energy spectra closely follows the experimental spectra. Nevertheless, at energies larger than 80 MeV/nucleon, QMD underpredicts the ^{7}Li energy spectra.

Using the same energy cuts in the GEMINI and QMD calculations as the experimental data, the isobaric ratios for $^{7}Li/^{7}Be$ and $^{10}Be/^{10}B$ were determined for $E_{\text{beam}}=33$ and 45 MeV/nucleon central collisions. Since QMD requires a significant amount of computational time to simulate a single event, a statistical population of ^{7}Be, ^{10}Be, and ^{10}B was hard to achieve for all the systems using the experimental angular widths. For that reason, the angular width was increased from the experimental width of 36°–44° to 30°–52°.

The left half of Fig. 9 are the ratios predicted at $E_{\text{beam}}=33$ MeV/nucleon, while the right half is the prediction at $E_{\text{beam}}=45$ MeV/nucleon. At $E_{\text{beam}}=33$ MeV/nucleon a single line (left solid) fits all of the experimental ratios while two lines are required to fit the $E_{\text{beam}}=45$ MeV/nucleon ratios (right solid). As expected, at both $E_{\text{beam}}=33$ MeV/nucleon and $E_{\text{beam}}=45$ MeV/nucleon, both GEMINI and BUU/GEMINI fail to predict a nonequilibrated system. But, BUU/GEMINI behavior deviates a great deal from the experimental ratios. For the ratios at $E_{\text{beam}}=33$ MeV/nucleon BUU/GEMINI ratios do not change significantly across the reacting systems.

GEMINI treats residues with similar compositions similarly; therefore, the products from the complete fusion resi-

TABLE II. Comparison of the residues determined by complete fusion with the residues predicted by BUU at $b=3$ and QMD at $b=0-3$, for the different reactions at $E_{\text{beam}}=33$, 45 MeV/nucleon.

		$\langle Z\rangle$	$\langle N\rangle$	$\langle A\rangle$	$\langle E^*/A\rangle$	$\langle N/Z\rangle$
		33 MeV				
GEMINI	Ca+Ni	48	50	98	5.5	1.04
	Ca+Fe	46	52	98	5.5	1.13
	Ar+Ni	46	52	98	5.5	1.13
	Ar+Fe	44	54	98	5.5	1.23
BUU, $b=3$	Ca+Ni	32	37	69	3.83	1.16
	Ca+Fe	32	37	69	3.81	1.16
	Ar+Ni	31	37	68	3.94	1.19
	Ar+Fe	30	38	68	3.47	1.27
QMD, preemission	Ca+Ni	0.66	0.48	1.14	0	0.73
	Ca+Fe	0.60	0.55	1.15	0	0.92
	Ar+Ni	0.60	0.55	1.15	0	0.92
	Ar+Fe	0.53	0.60	1.13	0	1.13
QMD, residues	Ca+Ni	39.5	43.7	83.2	4.9	1.11
	Ca+Fe	38.5	44.9	83.4	4.9	1.17
	Ar+Ni	38.3	44.4	82.7	4.9	1.16
	Ar+Fe	37.4	45.5	82.9	4.9	1.22
		45 MeV				
GEMINI	Ca+Ni	48	50	98	7.5	1.04
	Ca+Fe	46	52	98	7.5	1.13
	Ar+Ni	46	52	98	7.5	1.13
	Ar+Fe	44	54	98	7.5	1.23
BUU, $b=3$	Ca+Ni	27	30	57	4.9	1.11
	Ca+Fe	27	32	59	5.4	1.19
	Ar+Ni	26	31	57	5.3	1.19
	Ar+Fe	26	33	59	5.3	1.27
QMD, preemission	Ca+Ni	0.71	0.62	1.33	0	0.87
	Ca+Fe	0.67	0.67	1.34	0	1.00
	Ar+Ni	0.69	0.66	1.35	0	0.96
	Ar+Fe	0.61	0.72	1.33	0	1.18
QMD	Ca+Ni	31.6	36.1	67.7	5.9	1.14
	Ca+Fe	31.3	37.2	68.5	5.9	1.19
	Ar+Ni	31.4	37.4	68.8	5.9	1.19
	Ar+Fe	30.2	37.2	67.4	5.9	1.23

due from ^{40}Ca+^{58}Fe should be similar to the products from ^{40}Ar+^{58}Ni. However, the complete fusion residue of ^{40}Ar+^{58}Fe had 4 neutrons more than the complete fusion residue of ^{40}Ca+^{58}Ni. This difference is reflected in the increased production of neutron rich fragments in the ^{40}Ar+^{58}Fe case. At $E_{\text{beam}}=45$ MeV/nucleon, GEMINI and BUU/GEMINI's predictions of yield ratios are almost identical. Though the mass and excitation energy of the complete fusion and BUU's residues are very different, GEMINI predicted a very similar isobaric yield ratio. For GEMINI the ratio of the number of neutrons to protons in a residue is the primary factor that determined the composition of the reaction products when the excitation energy was above 5 MeV/nucleon rather than the mass or excitation energy of the residue.

Like GEMINI and BUU/GEMINI, QMD predicts an apparently equilibrated system. For $A=7$, QMD predicts the same trend as GEMINI. While the values of the ^{7}Li/^{7}Be ratio are slightly less than the ratio values predicted by GEMINI, both sets can be fit by a line with a similar slope of. For $A=10$ QMD reproduces the experimental results, within error bars, for all four systems at $E_{\text{beam}}=33$ MeV/nucleon and ^{40}Ca+^{58}Ni and ^{40}Ar+^{58}Ni at $E_{\text{beam}}=45$ MeV/nucleon. Except for reproducing the observed split and higher values with the ^{58}Fe target, QMD prediction agrees fairly well with the experimental data for the ^{10}Be/^{10}B ratio.

All the models seem to be underpredicting the value ofthe ^{7}Li yield. This is not surprising for BUU/GEMINI and GEMINI where prefragments are not included in the results. The composition of the QMD prefragments was primarily neutrons, protons, and alphas. QMD failed to produce a significant contribution of IMF as prefragments that might be present experimentally. At $A=10$ where contribution from prefragment emission is not as large of an issue, the isobaric ratios are closer to the experimental values.

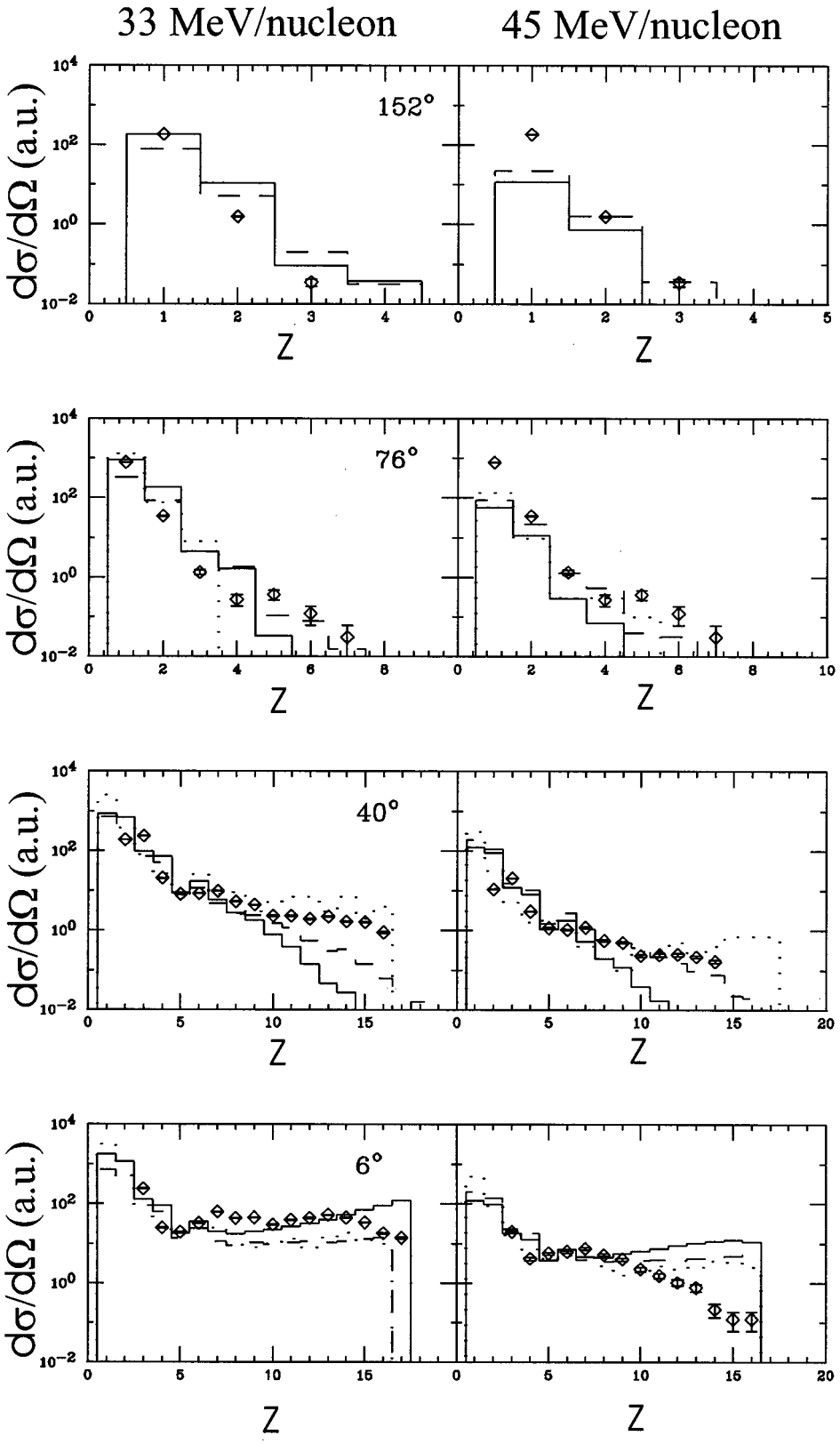

FIG. 7. Z distribution from $^{40}Ca+^{58}Fe$ at $E_{beam}=33$, 45 MeV/nucleon at $\theta_{lab}=6°$, 40°, 76°, and 152°; experimental (diamonds); QMD (dotted histogram); BUU/GEMINI (solid histogram); GEMINI (dashed histogram).

SUMMARY

In conclusion, isobaric beams from the K500 superconducting cyclotron have been used to study the effect of the neutron to proton ratio of the target and projectile upon the isobaric and isotopic composition of the emitted fragments. As reported earlier, at $E_{beam}=33$ MeV/nucleon the system is apparently chemically equilibrated prior to the emission of IMF's at 40°. When the energy is increased to $E_{beam}=45$ MeV/nucleon the system was not chemically equilibrated prior to the emission of IMF's at 40°. The isotopic

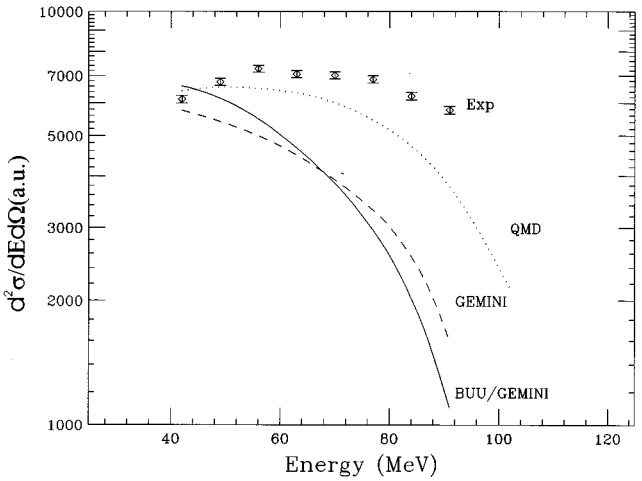

FIG. 8. Experimental ^{7}Li energy spectra at $\Theta_{lab}=40°$ (diamonds) compared to the predicted energy spectra of QMD (dotted), GEMINI (dashed), BUU/GEMINI (solid).

composition of fragments is dependent upon the angle of emission. This angular dependence is understood when one examines the moving source fits of the data. At $E_{beam}=33$ MeV/nucleon the fits showed that IMF's with $Z>3$ detected at intermediate angles were emitted from a single central source. At $E_{beam}=45$ MeV/nucleon there was a low energy contribution from the target source at intermediate angles. Both moving source fits and the isotopic ratios indicate that the fragments emitted at backward angles are dominated by emission from a targetlike source. When the slight contamination of the intermediate angle data by the targetlike source was removed by a neutron multiplicity cut the entrance channel dependence observed in the $Z=2$ ratios at 40° disappeared at $E_{beam}=33$ MeV/nucleon. At $E_{beam}=45$ MeV/nucleon the overall behavior remained the same.

In order to test the effect of known shortcomings in standard multifragmentation models, theoretical calculations were performed using GEMINI, BUU, and QMD. Overall, BUU input into GEMINI and GEMINI calculated from a complete fusion system failed to reproduce the experimental data. Both predict Maxwellian energy spectra for ^{7}Li at $\Theta_{lab}=40°$ that peak at about 40 MeV/nucleon and tail off rapidly, while the experimental energy spectra are fairly flat from 40 to 80 MeV/nucleon. In addition, when the isobaric ratios are plotted as a function of the system, GEMINI fails to reproduce the observed split in the $E_{beam}=45$ MeV/nucleon data, and the slope of the yield ratios at $E_{beam}=33$ MeV/nucleon is significantly different than the experimental data. On the other hand, QMD reproduces the experimental ^{7}Li energy spectra for 40–80 MeV/nucleon and the charge distribution from 6° to 76°. Like GEMINI, QMD fails to reproduce the observed split in the

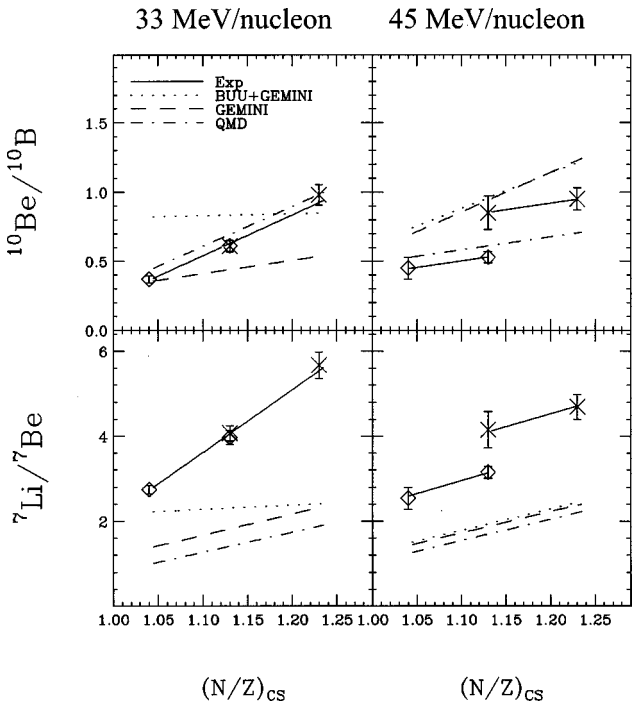

FIG. 9. Isobaric ratios at $\Theta_{lab}=40°$, for the 10% most central events, as a function of N/Z of the combined system at $E_{beam}=33$ (left side), 45 (right side) MeV/nucleon compared to the isobaric ratios predicted by GEMINI (dashed), BUU/GEMINI (dotted), and QMD (dashed dotted) (bottom) ^{7}Li/^{7}Be and (top) ^{10}Be/^{10}B.

$E_{beam}=45$ MeV/nucleon isobaric ratio plots, but, QMD reproduces the ^{10}Be/^{10}B isobaric ratios at 33 MeV/nucleon and ^{40}Ca+^{58}Ni and ^{40}Ar+^{58}Ni systems at $E_{beam}=45$ MeV/nucleon.

So while none of the calculations can reproduce the nonequilibrium nature of the reaction at $E_{beam}=45$ MeV/nucleon, QMD does reproduce ^{10}Be/^{10}B at the lower energy where the isotopic composition of fragments indicated the system is chemically equilibrated. This underscores the need for more dynamical formation of fragments in a model that has isospin dependence in the potential and the nucleon cross sections, allows for sequential decay. This is evident in the partial success of QMD in reproducing the data relative to either a purely statistical or hybrid calculation.

ACKNOWLEDGMENTS

This work was supported in part by the National Science Foundation under Grant Nos. PHY-9457376 and PHY-9509266, the U.S. Department of Energy under Grant No. DE-FG03-93ER40773, and the Robert A. Welch Foundation under Grant No. A-1266.

[1] J. Pochodzalla *et al.*, Phys. Rev. Lett. **75**, 1040 (1995).

[2] M. B. Tsang, F. Zhu, W. G. Lynch, A. Aranda, D. R. Bowman, R. T. de Souza, C. K. Gelbke, Y. D. Kim, L. Phair, S. Pratt, C. Williams, H. M. Xu, and W. A. Friedman, Phys. Rev. C **53**, R1057 (1996).

[3] F. Zhu, W. G. Lynch, D. R. Bowman, R. T. de Souza, C. K. Gelbke, Y. D. Kim, L. Phair, M. B. Tsang, C. Williams, and H. M. Xu, Phys. Rev. C **52**, 784 (1995).

[4] D. Morrissey, W. Benenson, and W. Friedman, Annu. Rev. Nucl. Part. Sci. **44**, 27 (1994).

[5] A. Kolomiets, E. Ramakrishnan, H. Johnston, F. Gimeno-Nogues, B. Hurst, D. O'Kelly, D. Rowland, S. Shlomo, T. White, J. Winger, and S. J. Yennello, Phys. Rev. C **54**, R472 (1996).
[6] S. J. Yennello, B. Young, J. Lee, J. A. Winger, J. S. Winfield, G. D. Westfall, A. Vander Molen, B. M. Sherrill, J. Shea, E. Norbeck, D. J. Morrissey, T. Li, E. Gualtieri, D. Craig, W. Benenson, and D. Bazin, Phys. Lett. B **321**, 15 (1994).
[7] H. Johnston, T. White, J. Winger, D. Rowland, B. Hurst, F. Gimeno-Nogues, D. O'Kelly, and S. J. Yennello, Phys. Lett. B **371**, 186 (1996).
[8] S. J. Yennello, B. Young, J. Yee, J. A. Winger, J. S. Winfield, G. D. Westfall, A. Vander Molen, B. M. Sherrill, D. J. Morrissey, W. J. Llope, T. Li, H. Johnston, E. Gualtieri, D. Craig, and W. Benenson, *Advances in Nuclear Dynamics* (World Scientific, Singapore, 1994), p. 63.
[9] W. Skulski *et al.*, Phys. Rev. C **53**, R2594 (1996).
[10] J. Toke, B. Djerround, W. Skulski, W. U. Schroder, D. K. Agnihotri, S. P. Baldwin, R. J. Charity, R. T. de Souza, B. Lott, B. M. Quednau, D. G. Sarentites, and L. G. Sobotka, *Advances in Nuclear Dynamics 2* (World Scientific, Singapore, 1996), p. 49.
[11] J. F. Dempsey, R. J. Charity, L. G. Sobotka, G. J. Kunde, S. Gaff, C. K. Gelbke, T. Glasmacher, M. J. Huang, R. C. Lemmon, W. G. Lynch, L. Manduci, L. Martin, M. B. Tsang, D. K. Agnihotri, B. Djerroud, W. U. Schroder, W. Skulski, J. Toke, and W. A. Friedman, Phys. Rev. C **54**, 1710 (1996).
[12] D. R. Bowman, G. F. Peaslee, R. T. de Souza, N. Carlin, C. K. Gelbke, W. G. Gong, Y. D. Kim, M. A. Lisa, W. G. Lynch, L. Phair, M. B. Tsang, C. Williams, N. Colonna, K. Hanold, M. A. McMahan, G. J. Wozniak, L. G. Moretto, and W. A. Friedman, Phys. Rev. Lett. **67**, 1527 (1991); D. R. Bowman, C. M. Mader, G. F. Peaslee, W. Bauer, N. Carlin, R. T. de Souza, C. K. Gelbke, W. G. Gong, Y. D. Kim, M. A. Lisa, W. G. Lynch, L. Phair, M. B. Tsang, C. Williams, N. Colonna, K. Hanold, M. A. McMahan, G. J. Wozniak, L. G. Moretto, and W. A. Friedman, Phys. Rev. C **46**, 1834 (1992).
[13] B. Libby, A. C. Mignerey, N. Colonna, P. Roussel-Chomaz, G. J. Wozniak, and L. G. Moretto, Phys. Rev. C **53**, 2993 (1996).
[14] S. Albergo, S. Costa, E. Costanzo, and A. Rubbino, Nuovo Cimento A **89**, 1 (1985).
[15] J. Aichelin, G. Peilert, A. Bohnet, A. Rosenhauer, H. Stocker, and W. Greiner, Phys. Rev. C **37**, 2451 (1988); J. Aichelin, Phys. Rep. **202**, 233 (1991).
[16] B. A. Li and D. H. E. Gross, Nucl. Phys. **A554**, 257 (1993).
[17] R. Charity *et al.*, Nucl. Phys. **A483**, 371 (1988).
[18] R. P. Schmitt, L. Cooke, G. Derrig, D. Fabris, B. Hurst, J. B. Natowitz, G. Nebbia, D. O'Kelly, B. K. Srivastava, W. Turmel, D. Utley, H. Utsunomiya, and R. Wada, Nucl. Instrum. Methods Phys. Res. A **354**, 487 (1995).
[19] T. C. White, H. Johnston, J. Winger, and S. J. Yennello, Texas A&M Progress in Research, 1994.
[20] E. Renshaw, S. J. Yennello, K. Kwiatkowski, R. Planeta, L. W. Woo, and V. E. Viola, Phys. Rev. C **44**, 2618 (1991).
[21] K. Kwiatkowski, J. Bashkin, H. Karwowski, M. Fatyga, and V. E. Viola, Phys. Lett. B **171**, 41 (1986).
[22] J. L. Wile *et al.*, Phys. Rev. C **45**, 2300 (1992).
[23] D. E. Fields, K. Kwiatkowski, D. Bonser, R. W. Viola, V. E. Viola, W. G. Lynch, J. Pochodzalla, M. B. Tsang, C. K. Gelbke, D. J. Fields, and S. M. Austin, Phys. Lett. B **220**, 356 (1989).
[24] J. R. Nix, Ann. Phys. (N.Y.) **41**, 52 (1967).
[25] L. G. Moretto, Nucl. Phys. **A247**, 211 (1975).
[26] J. Galin and U. Jahnke, J. Phys. G **20**, 1105 (1994).
[27] W. U. Schroeder, Nucl. Phys. **A538**, 439 (1992).
[28] R. Wada, R. Tezkratt, K. Hagel, F. Haddad, A. Kolomiets, Y. Lou, J. Li, M. Shimooka, S. Shlomo, D. Utley, B. Xiao, N. Mdeiwayeh, J. B. Natowitz, Z. Majka, J. Cibor, T. Kozik, and Z. Sosin, Phys. Rev. C **55**, 227 (1997).
[29] G. J. Kunde, S. Gaff, C. K. Gelbke, T. Glasmacher, M. J. Huang, R. Lemmon, W. G. Lynch, L. Manduci, L. Martin, R. Popescu, M. B. Tsang, J. Dempsey, R. J. Charity, L. G. Sobotka, D. K. Agnihotri, B. Djerroud, W. U. Schroder, W. Skulski, J. Toke, K. Wyrozebski, and D. Ruess, Phys. Rev. C **55**, R990 (1997).
[30] B. A. Li and S. J. Yennello, Phys. Rev. C **52**, R1746 (1995).
[31] J. P. Bondorf, A. S. Botvina, A. S. Iljinov, I. N. Mishustin, and K. Sneppen, Phys. Rep. **257**, 133 (1995).